

Local maximum entropy material point method applied to quasi-brittle fracture.

Miguel Molinos^{a1}, Pedro Navas^{a2}, Diego Manzanal^a, and Manuel Pastor^a

^a *ETSI Caminos, Canales y Puertos, Universidad Politécnica de Madrid.
c. Prof. Aranguren 3, 28040 Madrid, Spain*

Abstract

The objective of this work is to introduce an alternative technique to address the fracture process of brittle and quasi-brittle materials under the Material Point Method (MPM) framework. With this purpose the eigensoftening algorithm, developed originally for the Optimal Transportation Meshfree (OTM) approximation scheme, is extended to the MPM with the aim of presenting a suitable alternative to the existing fracture algorithms developed for such a methodology. The good fitting in the predictions made by the eigensoftening algorithm against both analytical and experimental results **proves** the excellent performance of the method when challenging applications are to modeled.

Keywords: Quasi brittle fracture, Local-*Max-Ent* approximation, Material Point Method, Solid Dynamics

Acronyms

EFGM Element-Free Galerkin Method. 2

FEM Finite Element Method. 2

LME Local Maximum-Entropy. 6, 7

⁵ **MPM** Material Point Method. 2–4, 7

OTM Optimal Transportation Meshfree. 2, 3

SPH Smoothed Particle Hydrodynamics. 2

¹Corresponding author: m.molinos@alumnos.upm.es

²Corresponding author: p.navas@upm.es

1. Introduction

The failure mechanisms of quasi-brittle materials and the crack propagation have been studied from different fields such as materials science, structural engineering, earth science and petroleum engineering . The prediction of crack propagation has been approached with different numerical techniques. The Finite Element Method (FEM) is widely used in industrial application. However, the presence of cracks is a violation of the continuity requirement of the FEM. To overcome this issue, numerous numerical **artifices** have been proposed with the aim of reproducing such a complex behaviour. These techniques vary from the employment of cohesive approaches [1, 2], or to the gradual insertion of cohesive elements [3, 4, 5] at solid elements boundaries. To alleviate these shortcomings of the FEM, the Extended Finite Element Method (XFEM) in conjunction with level set technique was introduced by Belytschko *et al.* [6] to handle arbitrary crack paths level set. Some relevant contributions to the XFEM are the modeling micro-scale crack propagation [7], the introduction of a cohesive zone model [8], and more recently improving it capability to predict the crack path in 3D cases [9].

The simulation of fracture propagation in a more accurate and effective way can be considered as one of the ongoing goals of the development of novel spatial discretisation methods like meshfree techniques. Some examples of it are the Material Point Method (MPM) [10, 11, 12, 13], the Element-Free Galerkin Method (EFGM) [14, 15, 16, 17], the Smoothed Particle Hydrodynamics (SPH) [18, 19], the Optimal Transportation Meshfree (OTM) [20, 21, 22, 23] or Peridynamics [24, 25] among others.

Concerning MPM, fracture has been treated numerically through two different ways. On the one hand, the “CRACKs with Material Points (CRAMP)” is proposed [12, 26]. The basis of this methodology consist of the removal of the restriction of the single-valued velocity field close to the crack through, at least, two sets of nodes. In this method, different labels are assigned to the material points and nodes to distinguish if they are in the same side of the crack or not. Under this approach, crack surface is described with line segments in 2D and triangle patches in 3D cases. The chosen criteria for crack propagation is based on such parameters as energy release rate analysed by Tan & Nairn (2002)[27], and the stress intensity factor or the J-integral discussed by Guo & Nairn (2004)[28]. On the other hand, the foundation of the second approach is the introduction of failed material points to describe the crack evolution. In these methods, the formation of failed points describes the nucleation of cracks, and thereafter its propagation and branching. Consequently, the position of the crack does not need to be explicitly stated.

This fact represents significant advantages over the “CRAMP”. Under this approach, the prediction of failure evolution is computed with a decohesion model, which has been discussed by Chen *et al.*[13] and Schreyer *et al.*[10]. Successful simulations are provided within the framework of the fracture of brittle materials by Chen *et al.* [11, 29] and Sulsky & Schreyer [30].

Similar to this approach, Schmidt *et al.* [31] introduced the concept of eigenfracture, where crack sets are approximated by means of eigen-deformations, which enable the material to develop displacement jumps at no cost of local elastic energy. Later, the eigenerosion approach to brittle fracture was carried out by Pandolfi *et al.* [32, 22]. In this technique, the concept of “erosion” of the material point is depicted, being the material point able to remain intact or become completely failed or eroded, when no loading capacity is bore. This method has been successfully applied to simulate high complex phenomena such as dynamic fragmentation of metals [23]. Recently, Zhang *et al.* [33] adopted the eigenerosion to resolve the dynamic fracture of brittle materials in the MPM framework. Nonetheless, when quasi-brittle materials are simulated though this approach, the results exhibit an overestimation of tensile stress and strain peaks. Furthermore, since the work of Zhang *et al.* [33] is made with conventional MPM/GIMP, stress oscillations are to be faced.

To overcome the limitations observed in the EigenMPM [33], the present research proposes the eigensoftening algorithm developed by Navas *et al.* [34, 35] for the OTM framework and engineered for quasi-brittle materials. Inspired in the concept of the crack band model [36], since energy dissipation is performed through the softened (or failed) volume, this methodology is able to capture the gradual rather than abrupt dissipation of the fracture energy. Moreover, in order to mitigate stress oscillations as well as to deal with tensile instabilities, such those that occurs when particles crosses an element boundary, the work of Molinos *et al.* [37] is followed. The traditional MPM technique is enhanced through the Local Maximum-Entropy (LME) approximation technique [38] for the spatial discretisation as well as a explicitly MPM Newmark Predictor-Corrector (NPC) scheme is derived for the time discretisation.

The paper is structured as follows. First meshfree methodology, eigen-erosion and eigensoftening algorithms are presented in Section 2. Then, both approaches are compared and verified by means of comparisons with analytical and experimental results in Section 3. Finally, relevant conclusions are exposed in Section 4.

2. The meshfree methodology

The aim of this section is to describe and introduce some special techniques required to face the fracture problem under the MPM framework. In consequence, this section is structured as follows: first, in 2.1, the Newmark Predictor-Corrector (NPC) algorithm for the MPM will be exposed; next the LME approximants are introduced in 2.2 as an accurate alternative technique to interpolate data between particles and nodes, and finally fracture algorithms based on the eigendeformation concept are presented in 2.3.

2.1. The MPM time integration : A Newmark Predictor-Corrector scheme

The MPM [39] is a meshfree Lagrangian-Eulerian method where the continuum Ω is discretised with a finite set of material points (also known as particles in this research) $\hat{\Omega} = \{\vec{x}_p, p \in \mathcal{C}\} \subset \Omega$, where $\mathcal{C} = 1, \dots, n_p$. Any particle field such as position, velocity, mass, volume and stress denoted by \vec{x}_p , \vec{v}_p , m_p , V_p and σ_p , respectively, are assigned to each material point. In addition to this set of material points, a set of fixed background nodes is introduced to compute the balance of momentum equation. This set of nodes is defined as $\mathbf{X} = \{\vec{x}_I, I \in \mathcal{B}\} \subset \mathbb{R}^2$, where $\mathcal{B} = 1, \dots, n_I$. In the present research, any nodal quantity is denoted by (\square_I) .

Since the MPM possesses the advantages of both Lagrangian and Eulerian descriptions, no element distortion takes place in the MPM. Therefore, it is an appropriate and efficient method to solve problems with moving discontinuities such as fracture evolution.

Without loosing generality, the MPM algorithm can be described with three main steps: (i) a variational recovery process, where particle data is projected to the grid nodes, (ii) an Eulerian step, where balance of momentum equation is expressed as a nodal equilibrium equation in a FEM-like procedure, and finally (iii) a Lagrangian advection of the particles. In the present research, the explicit predictor-corrector time integration scheme proposed by Molinos *et al.* [37] is adopted. The purpose of this choice is motivated due to its proved robustness and stability for dynamic computations. In the first stage, the nodal velocity predictor \vec{v}_I^{pred} is computed through particles velocities \vec{v}_p and accelerations \vec{a}_p and evaluated in the k time step,

$$\vec{v}_I^{pred} = \sum_{p \in \mathcal{C}} \frac{N_I(\vec{x}_p^k) m_p (\vec{v}_p^k + (1 - \gamma) \Delta t \vec{a}_p^k)}{m_I}. \quad (1)$$

Where γ is an user-defined parameter (typically adopted as 0.5), \mathbf{m}_I represents the lumped mass matrix, and $N_I(\vec{x}_p^k)$ is the nodal contribution of the shape function evaluated in the particle coordinates \vec{x}_p^k . This way of

computing the nodal predictor is numerically stable as well as minimises the computational effort. Once nodal velocities are obtained, the essential boundary conditions are imposed. After that, an Eulerian phase is computed in the set of nodes in a FEM-like way, where nodal forces \vec{f}_I^{k+1} are computed through the equilibrium equation. Next the nodal velocities are corrected in a *corrector* stage:

$$\vec{v}_I^{k+1} = \vec{v}_I^{pred} + \gamma \Delta t \frac{\vec{f}_I^{k+1}}{\mathbf{m}_I^k}. \quad (2)$$

Finally, in order to update the particles, those are advected in the Lagrangian stage as

$$\vec{a}_p^{k+1} = \sum_{I \in \mathcal{B}_p} \frac{N_I(\vec{x}_p^k) \vec{f}_I^k}{\mathbf{m}_I^k}, \quad (3)$$

$$\vec{v}_p^{k+1} = \vec{v}_p^n + \sum_{I \in \mathcal{B}_p} \Delta t \frac{N_I(\vec{x}_p^k) \vec{f}_I^k}{\mathbf{m}_I^k}, \quad (4)$$

$$\vec{x}_p^{k+1} = \vec{x}_p^n + \sum_{I \in \mathcal{B}_p} \Delta t N_I(\vec{x}_p^k) \vec{v}_I^k + \frac{1}{2} \Delta t^2 \frac{N_I(\vec{x}_p^k) \vec{f}_I^k}{\mathbf{m}_I^k}. \quad (5)$$

The complete pseudo-algorithm it is summarised in Appendix A.

2.2. Spatial interpolation technique : Local Maximum-Entropy approximants

Local Maximum-Entropy (LME) approximation scheme was introduced by Arroyo & Ortiz (2006)[38] as a bridge between finite elements and meshfree methods. The key idea under this interpolation technique is the interpretation of each nodal value N_I as a probability. Related with this definition, two important limits are introduced. First the maximum-entropy (*max-ent*) limit, which ensures a *unbiased statistical inference* based on the nodal data as states the Jayne's[40] principle of *maximum entropy*. And second the Delaunay triangulation that warranties the *least width* shape function support. To reach a compromise between two competing objectives, a Pareto set is defined as,

(LME) $_\beta$ For fixed \vec{x} minimise $f_\beta(\vec{x}_p, N_I) := \beta U(\vec{x}_p, N_I) - H(N_I)$

subject to
$$\begin{cases} N_I \geq 0, \quad I=1, \dots, n \\ \sum_{I=1}^{N_n} N_I = 1 \\ \sum_{I=1}^{N_n} N_I \vec{x}_I = \vec{x} \end{cases}$$

where $H(N_I)$ is the entropy of the system of nodes following the definition given by Shannon (1948) [41], the shape function width is defined as $U(\vec{x}_p, N_I) := \sum_I N_I |\vec{x}_p - \vec{x}_I|^2$, and β is a regularisation or *thermalization* parameter such that for Pareto optimal solutions $\beta \in (0, \infty)$. Notice that β has units of $[L]^{-2}$, therefore it can be controlled by adjusting a dimensionless parameter³, $\hat{\gamma} = \beta h^2$, where h is defined as a suitable measure of the nodal spacing. With the restrictions of the Pareto set, the unique solution of the local *max-ent* problem LME_β is,

$$N_I^*(\vec{x}) = \frac{\exp \left[-\beta |\vec{x} - \vec{x}_I|^2 + \vec{\lambda}^* \cdot (\vec{x} - \vec{x}_I) \right]}{Z(\vec{x}, \vec{\lambda}^*)}, \quad (6)$$

where $Z(\vec{x}, \vec{\lambda}^*)$ is the *partition function* defined as,

$$Z(\vec{x}, \vec{\lambda}) = \sum_{I=1}^{N_n} \exp \left[-\beta |\vec{x} - \vec{x}_I|^2 + \vec{\lambda} \cdot (\vec{x} - \vec{x}_I) \right], \quad (7)$$

and a Lagrange multiplier $\vec{\lambda}^*$ such minimise the function $\log Z(\vec{x}, \vec{\lambda})$. The traditional way to compute the optimal value of $\vec{\lambda}^*$ is through a Newton-Raphson procedure, or in more challenging scenarios by a combination of the Newton-Raphson and the Nelder-Mead Simplex algorithms [35]. Nonetheless, since finite strains are not involved in the present research, Newton-Raphson is an enough efficient method. For an uniform nodal spacing, β can be considered constant, thus first derivatives of the interpolation technique ∇N_I^* can be obtained by evaluating the following expression

$$\nabla N_I^* = -N_I^* (\mathbf{J}^*)^{-1} (\vec{x} - \vec{x}_I) \quad (8)$$

where \mathbf{J} is the Hessian matrix, defined by

$$\mathbf{J}(\vec{x}, \vec{\lambda}, \beta) \equiv \frac{\partial \vec{r}}{\partial \vec{\lambda}}, \quad (9)$$

$$\vec{r}(\vec{x}, \vec{\lambda}, \beta) \equiv \frac{\partial \log Z(\vec{x}, \vec{\lambda})}{\partial \vec{\lambda}} = \sum_I^{N_n} p_I(\vec{x}, \vec{\lambda}, \beta) (\vec{x} - \vec{x}_I). \quad (10)$$

An additional remark concerning the support of the interpolation function is that, in practice, the value of N_I decay exponentially following $\exp(-\beta \vec{r})$.

³To avoid confusion with the γ parameter of the NPC, the dimensionless parameter defined in Arroyo & Ortiz [38] as γ will be represent by $\hat{\gamma}$ to preserve as much as possible the original notation.

- 120 In this sense, a good practice is to truncate it under a tolerance (typically around 10^{-6}) that would ensure a reasonable range of neighbours, see [38] for details. This tolerance defines a limit value of the influence radius to find the neighbour nodes of a given integration point.

125 Within the context of MPM formulation, fracture can be modelled by failing particles according to a suitable failure criterion. When material points are failed, they are assumed to have null stress tensor. To reproduce this behaviour in the present research, the eigensoftening algorithm is introduced in the MPM framework as an alternative approach to the decohesion model
130 [13, 10]. The eigensoftening concept was originally developed by Navas *et al.* (2017)[34] as an extension for quasi-brittle materials of the eigenerosion proposed by Pandolfi & Ortiz (2012)[32] for fracture of brittle materials. The evaluation of both approaches [34] against experimental measures show that the eigenerosion algorithm significantly overestimates the tensile stress
135 and the strain peaks, meanwhile eigensoftening captures the forces and crack patterns accurately. Furthermore, the accuracy of this algorithm has been proven for complex fracture patterns such as the ones obtained with fiber reinforced concrete (FRC), [42].

The key idea behind the eigenerosion algorithm is the computation of the energy-release rate attendant to the failure of material point p ,

$$G_p^{k+1} = \frac{C_\epsilon}{m_p^{k+1}} \sum_{x_q^{k+1} \in B_\epsilon(x_p^{k+1})} m_q W_q^{k+1} \quad (11)$$

$$m_p^{k+1} = \sum_{x_q^{k+1} \in B_\epsilon(x_p^{k+1})} m_q \quad (12)$$

- 140 where $B_\epsilon(x_p^{k+1})$ is a n -dimensional sphere of radius ϵ centered at x_p^{k+1} . The particles which lie under this sphere are known as the ϵ -neighborhood of the material point (see [32]). This concept is conveniently sketched in Figure 1. Other parameters are the mass of the neighborhood m_p^{k+1} , the current free-energy density per unit mass W_q^{k+1} and the normalizing constant C_ϵ , which
145 also defines the ϵ -neighborhood size, being $\epsilon = C_\epsilon h$, and h is a measure of the distance between nodes.

150 The failure criterion consist of considering that a material point is failed when G_p^{k+1} surpasses the critical energy release rate that measures the material-specific energy, G_F . The convergence of this approach has been analyzed by Schmidt *et al.* (2009)[31], who proved that G_F converges to the Griffith

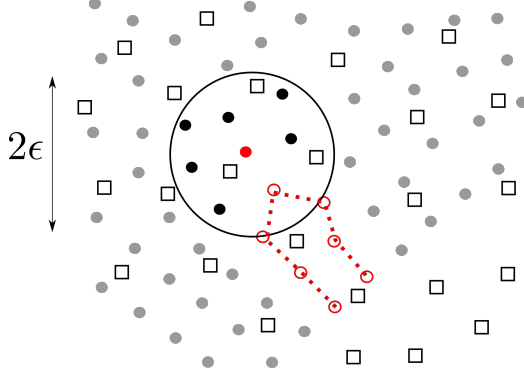


Figure 1: Scheme of a linear cohesive law, where the shaded area is G_f , f_t is the tensile strength, and w_c is the critical opening displacement.

fracture when the discretisation size tends to zero. It is necessary to point out that, when a material point overpass the critical energy, its contribution to the internal forces vector is set to zero, but its contribution to the mass matrix is preserved.

155

As can be noticed, the eigenerosion algorithm relies over an energetic failure criterion. Because of this, unrealistic stress concentration (higher than tensile strength) appears in quasi-brittle materials [34]. To overcome this limitation, the aforementioned authors proposed the concept of eigensoftening to take into account the gradual failure in quasi-brittle materials. The idea behind this concept is inspired in the cohesive fracture. This gradual failure criterion is plotted in Figure 2, where a linear decreasing cohesive law is presented to illustrate the concept earlier described. In the picture, the shaded region represents the static fracture energy per unit of area, G_F . Notice how a cohesive crack appears when the maximum tensile strength, f_t , is reached. Once the crack, w_n , reaches the value of the critical crack opening, w_c , a stress-free crack is attained. For the eigensoftening algorithm, a strength criterion for crack initialization was adopted. Particularly the maximum principal stress theory for brittle fracture was considered in [34], this allows to quantify the variation of the averaged strain energy density in the ϵ -neighborhood of the material point \bar{x}_p^{k+1} as

$$\delta W_{\epsilon,p} = \frac{\partial G_p}{C_\epsilon} = \frac{1}{m_p} \sum_{x_q^{k+1} \in B_\epsilon(\bar{x}_p^{k+1})} m_q \sigma_{q,I} \delta \varepsilon_q, \quad (13)$$

where $\sigma_{q,I}$ is the maximum principal stress of each material point in the ϵ -neighborhood. At this point, an *effective* strain ε_q is introduced in order to obtain the variation of the local strain energy as $\delta W_q = \sigma_{q,1} \delta \varepsilon_q$. Now,

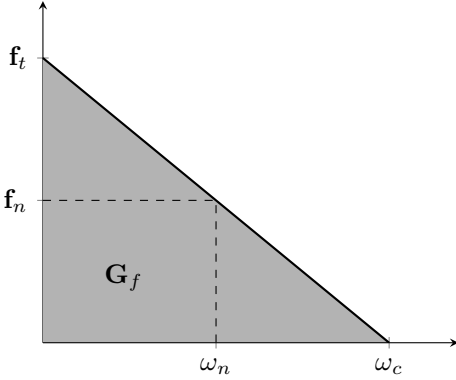


Figure 2: Scheme of a linear cohesive law, where the shaded area is G_f , f_t is the tensile strength, and w_c is the critical opening displacement.

with the assumption that the effective strain of each material point at every time step is constant in the neighbourhood of \vec{x}_p^{k+1} , the equation (13) can be simplified to

$$\delta W_{\epsilon,p} = \frac{\delta \epsilon_p}{m_p} \sum_{x_q^{k+1} \in B_\epsilon(x_p^{k+1})} m_q \sigma_{q,I}. \quad (14)$$

Consequently, it is possible to define an equivalent critical stress at the material point \vec{x}_p^{k+1} as

$$\sigma_{\epsilon,p} = \frac{1}{m_p} \sum_{x_q^{k+1} \in B_\epsilon(x_p^{k+1})} m_q \sigma_{q,I}, \quad (15)$$

where m_p is the total mass of the ϵ -neighborhood, defined similarly to the eigenerosion method (Eq. (12)). The equivalent critical stress leads to a definition of the averaged strain energy in terms of the averaged strain as $\delta W_{\epsilon,p} = \sigma_{\epsilon,p} \delta \epsilon_p$. The softening behaviour is activated once $\sigma_{\epsilon,p}^{k+1}$ surpasses the tensile strength, f_t . This consists of a reduction of the internal forces as,

$$f_I^{int} = \sum_p (1 - \chi_p) \sigma_p^{k+1} \cdot \text{grad}(N_{Ip}) \Omega_p, \quad (16)$$

where χ_p and Ω_p are respectively the damage or softening variable and the volume for each material point p . χ_p is any function, taking values between zero (an intact material) and one (completely failed material points), that relates the crack opening and the residual strength. To calculate it, typical

shapes of cohesive laws such as linear, bilinear or exponential, may be employed. For the case of a linear softening such the sketched one in the Figure 2, χ_p is computed as,

$$1 - \chi = \frac{f_n}{f_t} = 1 - \frac{w_n}{w_c} \rightarrow \chi = \frac{w_n}{w_c}. \quad (17)$$

Analogous to the crack band model presented by Bazant [36], Navas *et al.* [42] [34] introduced a band width parameter h_ϵ in order to relate the crack opening with the strain. Concerning this parameter, a typical value between two and four times the maximum size of the aggregates is adopted in the case of concrete as brittle material. The effective fracture strain $\varepsilon_{\epsilon,f}$ is defined as the difference between the strain at crack initialization, $\varepsilon_1(\vec{x}_p^0)$, and the current strain, $\varepsilon_1(\vec{x}_p^{k+1})$, for a material point p . Also, $\varepsilon_{\epsilon,f}$ can be represented as the current crack opening w_n within the band width h_ϵ . Therefore,

$$\varepsilon_{\epsilon,f} = \varepsilon_1(\vec{x}_p^{k+1}) - \varepsilon_1(\vec{x}_p^0) = \frac{w_n}{h_\epsilon} \quad (18)$$

Introducing (18) in (17), the damage variable can be computed as,

$$\chi = \frac{\varepsilon_{\epsilon,f} h_\epsilon}{w_c}. \quad (19)$$

The function of χ presented in (19) represents a linear softening behaviour. For a general case, the damage variable can be expressed in terms of the following variables,

$$\chi = \chi(\varepsilon_{\epsilon,f}, h_\epsilon, f_t, w_c, G_f) \quad (20)$$

Implementation details can be consulted in Appendix B.

2.4. ϵ -neighbourhood reconstruction : A node-linked method

The construction of the ϵ -neighbourhood is a major issue of the proposed methodology. Since this operation could be extremely demanding, optimal numerical implementation should be employed. In opposite with the Cell-linked method proposed by Allen & Tildesley [43] where the definition of a numerical tolerance is required for auxiliar algorithms like Crossing Number [44] or Correct Even-Odd [45], the proposed methodology adopted herein is linked to the shape function neighbourhood. In order to avoid the aforementioned error prone techniques, we endeavour to exploit the meshfree benefits of the LME approximants to introduce a node-linked method. Due to the global support of this interpolation technique, the classical interpretation

of the FEM element typically adopted in MPM simulations is not required anymore. Instead, a linked list with the surrounding nodes for each node is
 170 defined at the initial time. Also, each particle has to be associated with the closest node instead of with the belonging element as heretofore has been done. Now lets define the concept of a particle *tributary nodes* as the list of nodes close to it among which the information transfers occurs. Once the closest nodes are defined, the particle possesses automatically a list of
 175 *tributary nodes*. This has two immediate benefits: the first one is that shape functions with global support as LME are easier to be implemented, and the second one is the increase of the efficiency of the ϵ -neighbourhood reconstruction. Regarding this last benefit, since the current particle has a *tributary nodes* list assigned to it, and consequently each node has a linked
 180 list with a set of *tributary particles*⁴ close to it, it is possible to define efficiently a search list with those particles close to the current particle. In the end, particles out of the area of influence, Figure 1, are pop out of the final ϵ -neighbourhood. A final remark about this new approach is its ability to reconstruct easily a search list with the support of the initial connectivity of
 185 the mesh. It provides a suitable basis for an easy implementation of other interpolation techniques with minimum coding effort. A detailed explanation of the proposed algorithm can be found in Appendix C.

3. Cases of study and discussion

The proposed approach to overcome the two main shortcomings of Eighen-
 190 MPM has been evaluated with three benchmark tests. On the one hand, the benchmark proposed in section 3.1 discuss the presence of stress instabilities provoked by the spatial discretisation. For that purpose, two different interpolation techniques, GIMP and LME, as been compared by carrying out an eigenerosion simulation. And on the other hand the inability of the eigen-
 195 erosion to simulate properly quasi-brittle fracture is discussed in sections 3.2 and 3.3, where experimental results are compared with numerical ones. In the first case comparing with a semicircular bending test and in the second case with a drop-weight impact test.

3.1. Edge-cracked square panel in mode I

The aim of the problem presented hereinafter is to assess the capability of the LME approximants to improve the result *versus* the standard linear interpolation and uGIMP [47]. The application consists of a square plate of
 200

⁴Notice that the list of the particles close to each node is unique for each node and is updated in each time step.

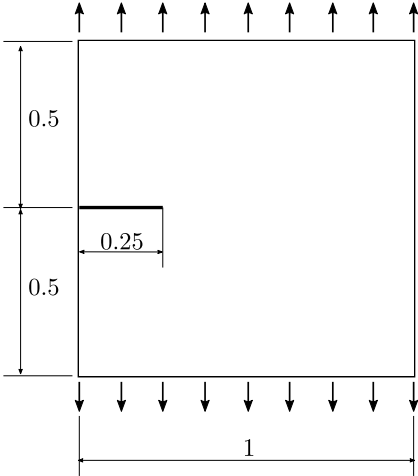


Figure 3: Geometry and boundary condition of the drop-weight impact test.

size $H = 1$ containing an initial edge crack of length $0.25 \cdot H$ loaded in a pure mode I by displacement control on the outer flanks of the plate (See 205 Figure 3 for details). The constitutive model considered in the numerical experiment is a linear-elastic Hookean material, whose Young's modulus $E = 1.06$, the Poisson's ratio $\nu = 0.333$, and critical energy-release rate $G_F = 0.0001$. The absence of units is due to the current simulation will not be tested against experimental results, where scale factor is relevant, but will 210 be validated against an analytical solution provided by Pandolfi & Ortiz [32]. In MPM, two different discretisation are required. On one hand, a cartesian grid of nodes is considered with a nodal spacing value of 0.025. On the other hand, the plate will be modeled with a initial layout of four particles per element and occupying the Gauss quadrature positions.

215 Figure 4 clearly shows that the LME $_{\gamma=3.5}$ solution has a reaction peak value of 0.03 for a imposed displacement 0.015 which agrees with the analytical solution [32]. It also shows the presence of wiggles in the reaction-displacements curve, in both loading and post-failure stages, when linear 220 interpolation technique is used. In contrast, LME simulation does not exhibit these spurious oscillations and remains linear until the failure. About the strength, linear interpolation produces stiffer results than LME. This can be attributed to imprecision in the stress field due to grid-crossing phenomena. Alternative to LME, uGIMP shape functions can be employed to 225 mitigate grid-crossing instabilities. Figure 4 supports this fact since it does not exhibit instabilities when particles cross element borders meanwhile these instabilities are found with linear interpolation. Unfortunately, the extended

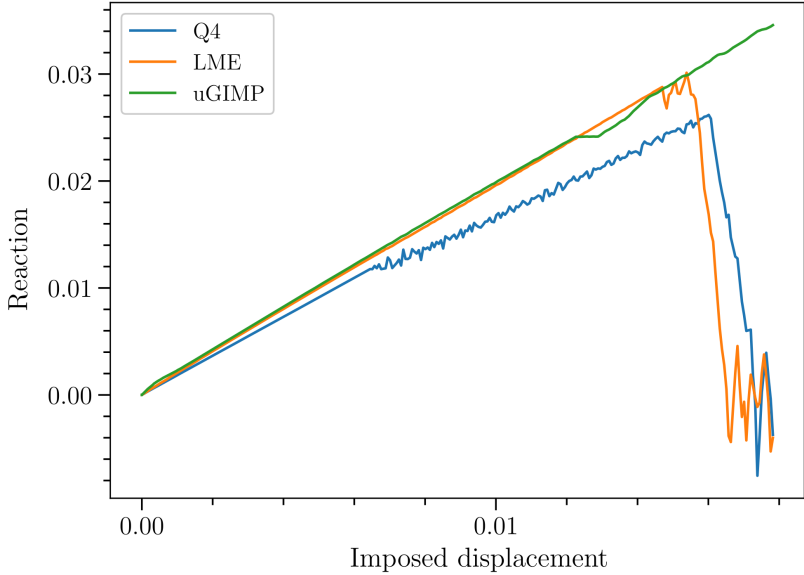
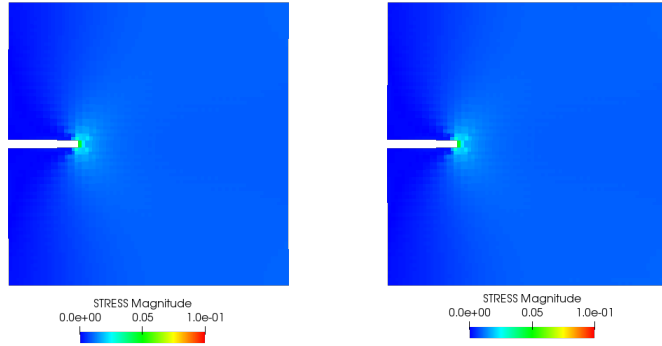


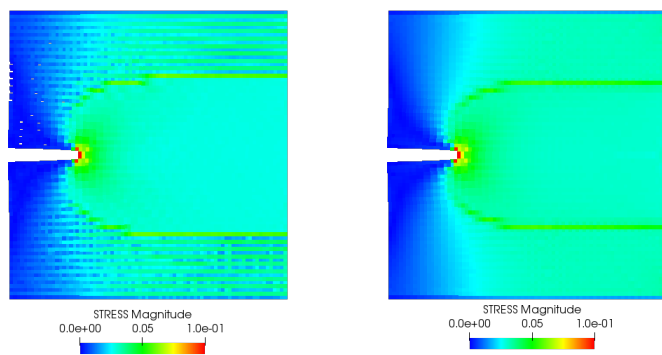
Figure 4: Evolution of the reaction forces plotted *versus* the imposed displacement for linear interpolation technique and the LME approximants.

support of this kind of shape function interfere with nodes in both sides of the notch, producing an undesired “tie-effect”. This involves in a violation
230 of the free border boundary condition in the notch. Possible solutions to this effect are the suppression of the elements in the notch, within a CRAMP-like method where two pairs of nodes are employed, or reducing the mesh size. With LME approximants these artefacts are not required since it is possible to control the support of the shape function reducing the grid-crossing and
235 avoiding the “tie-effect” in the notch at the same time.

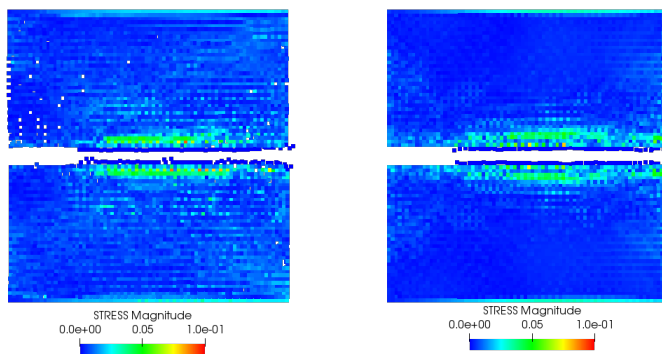
Additionally, Figure 5 remark clearly the difference between linear interpolation and LME, since numerical instability becomes rather significant when particles crosses the boundary of the element in the linear case, which is observed at 60 seconds. Although, apparently, the differences in the obtained
240 peaks are not extremely significant, it can be owing to the aforementioned hookean material employed [33]. When more sophisticated constitutive models will be employed, severe inaccuracies may appear in the stress field that could affect dramatically to the final result. Focusing on the post failure behavior, it can be seen how LME produces soft stress field evolution even after
245 breaking. An important consideration regarding the presence of oscillations once both parts of the panel are separated is observed in Figure 4. These phenomena should not be attributed to the eigenerosion algorithm since the fracture process is over. They are due to the dynamic nature of the solver:



(a) $t = 25$



(b) $t = 60$



(c) $t = 100$

Figure 5: Evolution of the stress tensor magnitude for linear interpolation (pictures in the left side), and LME (pictures in the right side). **The results are printed directly on the material points.**

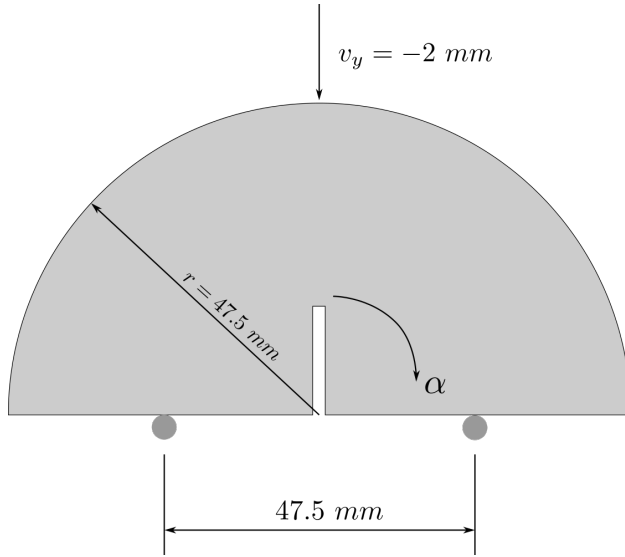


Figure 6: Geometry and boundary condition of the semicircular bending test.

once the energy is released dinamically by the crack, the waves propagate
250 along the domain.

3.2. Semicircular bending test

The second application to be considered analyses the bending behavior of semicircular specimens of Johnstone rocks, text which were experimentally carried out by Lim *et al.* [48] and numerically reproduced by Wang *et al.*[18]
255 under SPH framework within an implicit algorithm. The aim of the test is to examine the predictive capability of the eigensoftening algorithm under different kind of mixed-mode loading conditions. This capability was assessed previously within a OTM implementation [42].

The geometry and boundary conditions are sketched in Figure 6. The
260 experiment consist of loading semicircular specimens with a radius of 47.5 mm and a thickness of 20 mm, supported by two rollers at a span of 47.5 mm, by another roller on its top mid-span. Notches with a length of 16.6 mm are created with the different notch angles of 0° , 30° and 60° with respect to the vertical axis in order to investigate the influence of the notch angle on the
265 peak load 8. The material properties of Johnstone rock are listed in Table 1. In the tests, particles were uniformly distributed with an almost constant separation of 1 mm between them, resulting in a total number of 4672 MPM particles for generating the specimen. Additionally, a regular cartesian background grid of 1917 nodes with 1.5 mm of nodal distance was generated. The
270 velocity of the top boundary particles is $v_y = 2 \text{ mm/s}$, whereas the velocity

Young's modulus (E)	0.4 GPa
Poisson ratio (ν)	0.25
Density (ρ)	1.54 g/cm ³
Tensile strength (f_t)	0.6 MPa
Critical opening displacement (w_c)	0.015 mm

Table 1: Material properties of Johnstone.

of the bottom boundary particles is $v_y = 0\text{mm/s}$. To reduce dynamic effects due to a sudden loading, a soft loading ramp has been employed as a loading curve. Finally, the model was calibrated with a regularization parameter $C_\epsilon = 1.7$ and a bandwidth value $h_\epsilon = 15$.

Figure 7 shows the comparison of mixed-mode fracture envelope between experiments and MPM simulations for different notch inclination angles $\alpha = 0^\circ$, 30° and 60° . The final fracture pattern is a vertical straight line when $\alpha = 0^\circ$ (pure mode I). When $\alpha > 0^\circ$, the sample is subjected to a mixed-mode pattern. For the cases of 0° and 30° , cracks initiate from the notch tip and then propagate towards upper loading point. Experiments show that a few cracks tend to initiate behind notch tip when the notch angle is beyond 50° . Figure 7 demonstrates that eigensoftening, combined with MPM, is able to reproduce this behavior. Therefore, the simulation results predict successfully the fracture envelope in experiments and demonstrate the capability of the eigensoftening-MPM model for capturing the fracture development under various complex loading conditions. Additionally, 8 compare the peak load between experiments and simulations for the notch inclination angles 0° , 30° and 60° . This figure proofs how the eigensoftening-MPM simulation can appropriately capture the increasing trend of the peak load with the increasing notch angles in the experiment.

3.3. Drop-weight impact test

This section is devoted to proof the accuracy of the eigensoftening algorithm within the MPM framework when the behavior of quasi-brittle materials under dynamic loading is simulated. One of the most interesting examples of this loading case is the three-point bending test on a concrete notched beam when it is conducted under impact loading. Indeed, this experimental test is appropriate to be reproduced numerically with the explicit solver proposed in this paper since fracture occurs in a period of milliseconds and waves propagate fast along the high strength materials involved in the aforementioned test. Accordingly, small time steps are required to achieve a numerically stable simulation.

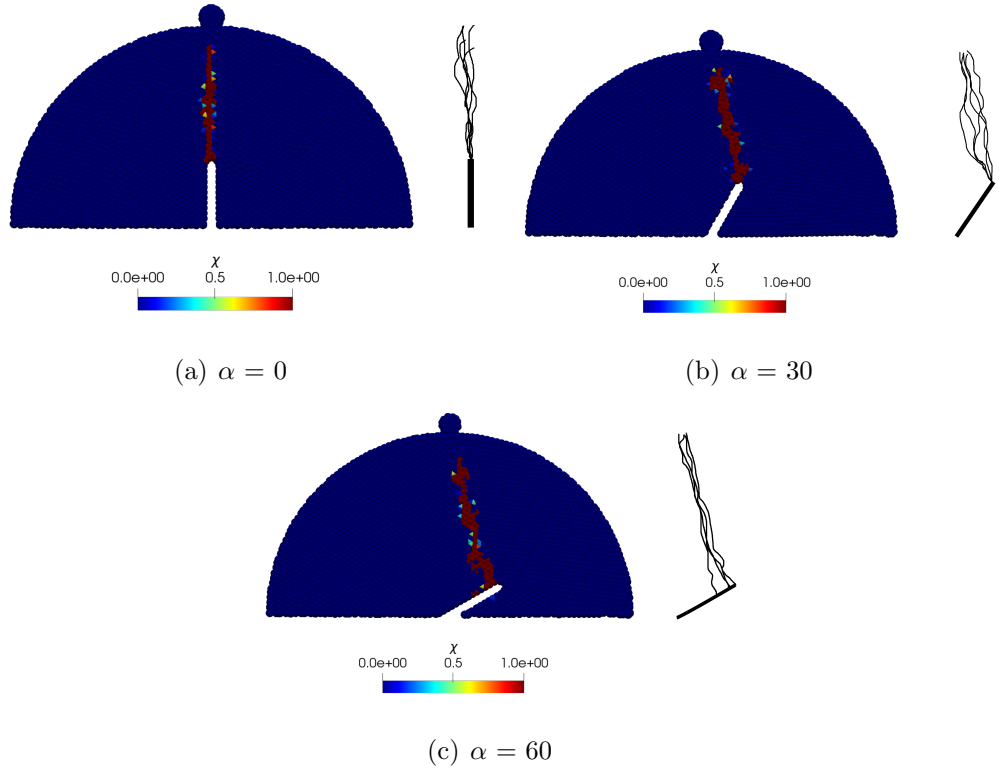


Figure 7: Crack pattern for different notch inclination angle, and comparison with the experimental results [48]. [The results are printed directly on the material points.](#)

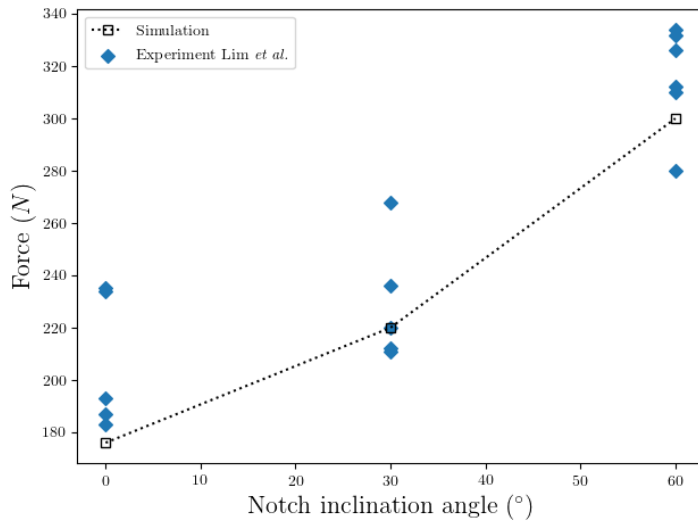


Figure 8: Numerical results compared with the experimental results [48].

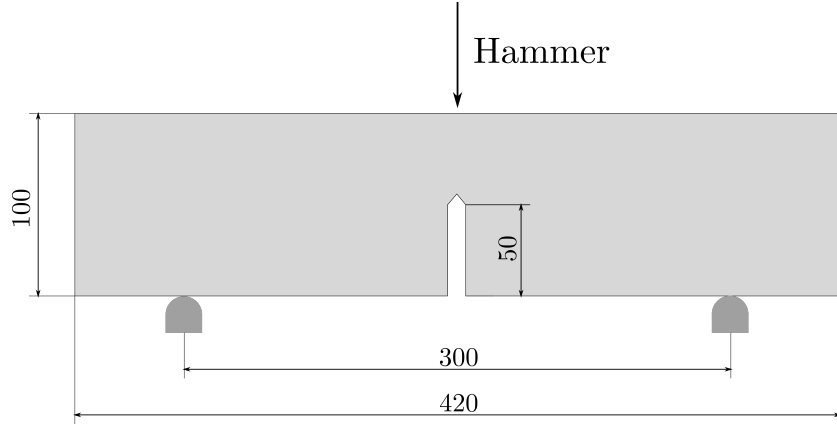


Figure 9: Geometry and boundary condition of the drop-weight impact test.

	ρ (kg/m ³)	f_c (MPa)	f_t (MPa)	G_F (N/m)	E (GPa)	d_{max} (mm)
Value	2368	102.7	5.4	141	31	12

Table 2: Mechanical properties of the high strength concrete.

An interesting case of this experimental test was reported by Zhang *et al.* [49, 50]. As in the aforementioned study, an impact hammer of 120.6 kg has been employed in the proposed simulations to drop it at an impact speed of 2640 mm/s. The beam dimensions were 100 mm x 100 mm (B x D) in cross section, and 420 mm in total lenght (L). The initial notch-depth ratio was approximately 0.5, and the span, S, was fixed at 300 mm during the tests (see Figure 9). The material adopted for the simulation was characterised by Navas *et al.* [34], being the material properties, such as the material density, ρ , the compressive strenght, f_c , the tensile strenght f_t , the specific fracture energy, G_F , and the elastic modulus E, provided in table 2.

For the present research, a 2D setting of the experiment has been adopted. Both the hammer and the concrete beam are explicitly represented in order to properly capture the impact. Several levels of discretisation were required to assess the objectiveness of the obtained results. The results here exposed are from a discretisation of 21576 material points and 3943 nodes. To achieve better results, an unstructured grid layout has been adopted focusing the minimum nodal spacing, 1.2 mm, in the middle of the beam and in the impact surface of the hammer. For this simulation, $\hat{\gamma}$ was fixed to 1.8, this low value of the regularization parameter smooth high stress overshoots after the impact. Here the stabilization properties of the LME described in [37]

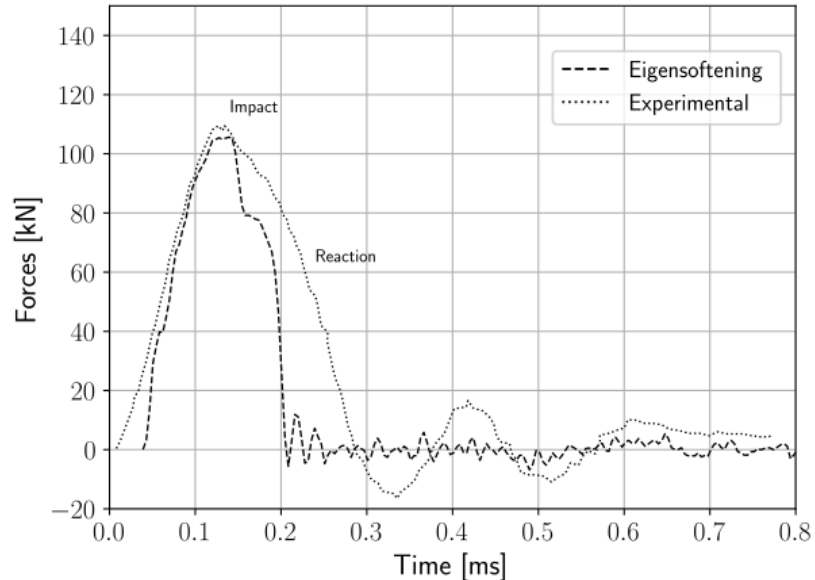
325 becomes crucial to achieve non-spurious results. In fact, standard linear element were tested with unsatisfactory results since grid-crossing occurs in the hammer head producing non realistic forces.

330 First, the reaction and impact forces are validated against their experimental counterparts. Since the impact forces applied by the hammer and
335 the reaction forces at the two supports were experimentally measured, they are compared with numerical ones in Figure 10. Note that the general trend of the impact forces was correctly captured. Although the traditional MPM implementation allows collision of two bodies, inaccurate energy conservation is obtained without the implementation of a conservative contact algorithm
340 to reproduce the hammer impact in the beam. Despite the observed discrepancies, this is out of the scope of this document, although future research of authors will overcome this limitation. Similarly, results of support forces will be more realistic when modelled by a suitable contact algorithm instead of avoiding any vertical displacement. Navas *et al.* (2017)[34] demonstrate
345 the importance of the stiffness of the support in order to obtain accurate results of the reaction forces. Interesting contact algorithms within the MPM methodology are available in the literature [51, 52].

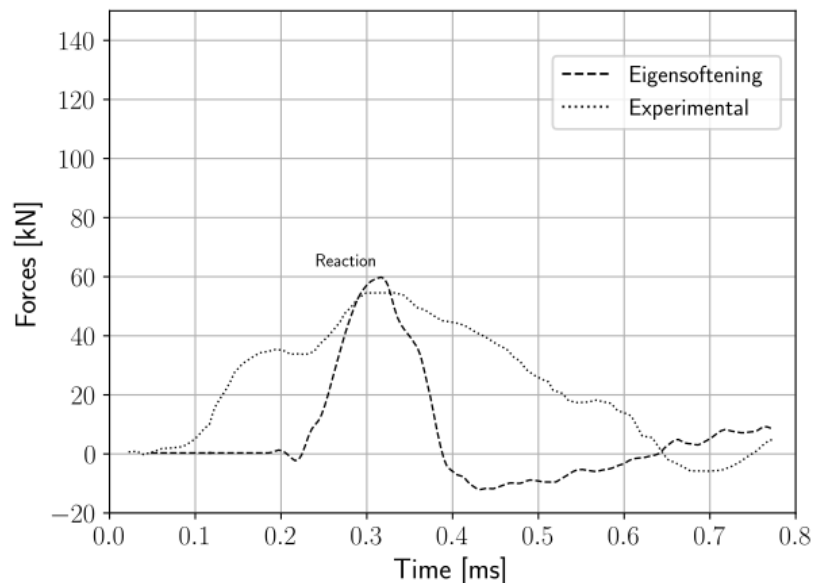
350 Finally, longitudinal stress distribution and crack propagation are depicted in Figure 11. Stress evolution agrees with the results obtained by [34] under the OTM framework. Two additional considerations about this results are concerning the interpolation technique. On the one hand, in the opposite to the uGIMP shape function, LME allows unstructured grids. This is a remarkable benefit for this kind of simulations since the majority of the computational effort is clearly localised in a tiny region of the domain. On the other hand, there is the possibility to reduce the shape function support to avoid a material point in one side of the crack is affected by those in the other side of the crack.

4. Conclusions

355 The paper proposes the eigensoftening algorithm in a MPM framework for quasi-brittle materials to overcome the limitations observed in the EigenMPM [33]. The overestimation of tensile stress and strain peaks in the fracture mechanism of quasi-brittle materials and the stress oscillations observed with conventional MPM are faced. Based on the EigenMPM approach to fracture, two additional improvements have been proposed in the present research in order to solve the shortcomings of the original concept pointed out
360 in the aforementioned paper [33].



(a) Hammer forces



(b) Reactions

Figure 10: Comparison of eigensoftening *versus* experimental results.

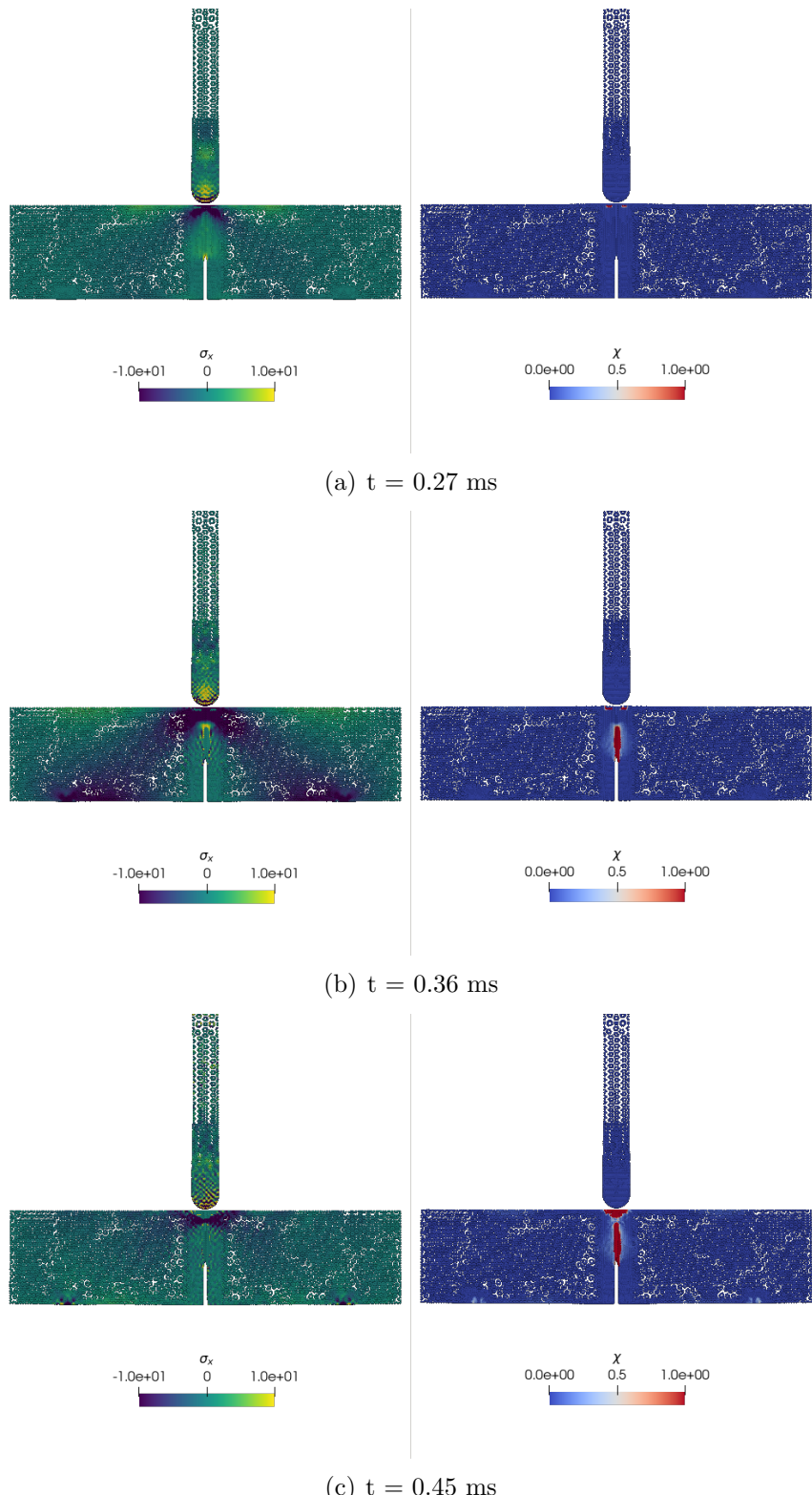


Figure 11: Evolution of the stress tensor magnitude [MPa] for linear interpolation (pictures in the left side), and LME (pictures in the right side). The results are printed directly on the material points.

Firstly, by introducing the concept of eigensoftening to the MPM framework, which allows to consider gradual failure process of each material point. This concept is analogous the softening law which is traditionally employed in the context of cohesive fracture in FEM. Furthermore, this failure criterion admits the design of more elaborated damage curves, which can be employed in order to describe the failure process in more sophisticated materials. Secondly to achieve better results, three new numerical algorithms has been implemented. The LME approximants are employed to remove from the solution those wiggles provoked by inaccuracies in the stress integration and to avoid the “tie-effect” observed in the uGIMP. The traditional time scheme of the MPM has been improved with a Newmark Predictor Corrector scheme as well. And the traditional concept of element connectivity has been removed to allow a more flexible and efficient implementation of search algorithm. In this research, the aforementioned techniques have helped to improve the results in fracture propagation through the eigensoftening and eigenerosion algorithms.

Finally, further improvements of the present research are exposed. The algorithm would have the ability to simulate of crack patterns in composite material such as steel or carbon fiber reinforced concretes[42, 53]. In addition, the eigensoftening approach can be extrapolated to rock fracture in the same manner the eigenerosion was [54], taking into account that the volumetric stiffness remains in order to support bulk loads. Also the benefits of LME can be exploited by adapting it through the deformation gradient [55]. *A priori* this would enhance the localisation properties of the proposed algorithms in more sophisticated domains. And the implementation of a contact algorithm to model other impact cases such as bullets collisions.

Acknowledgements

The financial support to develop this research from the Ministerio de Ciencia e Innovación, under Grant No. BIA-2016-76253 is greatly appreciated. The first and the second authors also acknowledge the fellowship Fundación Agustín de Betancourt and Juan de la Cierva (FJCI-2017-31544) respectively.

Acronyms

EFGM Element-Free Galerkin Method. 2

FEM Finite Element Method. 2

LME Local Maximum-Entropy. 6, 7

MPM Material Point Method. 2–4, 7

OTM Optimal Transportation Meshfree. 2, 3

⁴⁰⁰ **SPH** Smoothed Particle Hydrodynamics. 2

Appendix A. Explicit Newmark Predictor-Corrector algorithm

1 Update mass matrix : $\mathbf{m}_I = N_{Ip}^k m_p$

2 Explicit Newmark Predictor :

$$\vec{v}_I^{pred} = \sum_{p \in \mathcal{C}} \frac{N_I(\vec{x}_p^k) m_p (\vec{v}_p^k + (1 - \gamma) \Delta t \vec{a}_p^k)}{m_I}$$

3 Impose essential boundary conditions : At the fixed boundary, set $\vec{v}_I^{pred} = 0$.

4 Deformation tensor increment calculation :

$$\Delta \varepsilon_p^{k+1} = \Delta t \dot{\varepsilon}_p^{k+1} = \sum_{I \in \mathcal{B}_p} \Delta t \left[\vec{v}_I^{pred} \otimes \text{grad}(N_I(\vec{x}_p^k)) \right]^s$$

5 Update the density field : $\rho_p^{k+1} = \frac{\rho_p^k}{1 + tra[\Delta \varepsilon_p^{k+1}]}$.

6 Compute stress field and update damage parameter

7 Balance of forces calculation : Calculate the total grid nodal force $\vec{f}_I^{k+1} = \vec{f}_I^{int,k+1} + \vec{f}_I^{ext,k+1}$.

8 Explicit Newmark Corrector :

$$\vec{v}_I^{k+1} = \vec{v}_I^{pred} + \gamma \Delta t \frac{\vec{f}_I^{k+1}}{\mathbf{m}_I^{k+1}}$$

9 Update particles lagrangian quantities :

$$\vec{a}_p^{k+1} = \sum_{I \in \mathcal{B}_p} \frac{N_I(\vec{x}_p^k) \vec{f}_I^k}{\mathbf{m}_I^k}$$

$$\vec{v}_p^{k+1} = \vec{v}_p^n + \sum_{I \in \mathcal{B}_p} \Delta t \frac{N_I(\vec{x}_p^k) \vec{f}_I^k}{\mathbf{m}_I^k}$$

$$\vec{x}_p^{k+1} = \vec{x}_p^n + \sum_{I \in \mathcal{B}_p} \Delta t N_I(\vec{x}_p^k) \vec{v}_I^k + \frac{1}{2} \Delta t^2 \frac{N_I(\vec{x}_p^k) \vec{f}_I^k}{\mathbf{m}_I^k}$$

10 Reset nodal values

Algorithm 1: Explicit Newmark Predictor-Corrector scheme

Appendix B. Eigensoftening Algorithm

```

Input: For each  $p$ ,  $\epsilon$ -neighbourhood,  $f_{t,p}$ ,  $h_{\epsilon,p}$ ,  $w_c$ 
Output: Return damage parameter  $\chi = \{\chi_p\}$ 
Data: Testing set  $x$ 

1  $\chi_p \leftarrow \chi_p^k$ 
2 for  $p$  to  $N_p$  do
3   if  $\chi_p = 0$  and  $\epsilon_{f,p} = 0$  then
4     for  $q \in B_{\epsilon,p}$  do
5        $\sigma_{q,I} \leftarrow \text{getEigenvaluesOf}(\sigma_q)$ 
6       if  $\chi_q < 1$  then
7          $\sum m_p \sigma_{p,I} \leftarrow \sum m_p \sigma_{p,I} + m_q \sigma_{q,I}$ 
8       end
9        $m_p \leftarrow m_p + m_q$ 
10      end
11       $\sigma_{p,\epsilon} \leftarrow \frac{1}{m_p} \sum m_p \sigma_{p,I}$ 
12      if  $\sigma_{p,\epsilon} > f_{t,p}$  then
13         $\epsilon_{f,p} = \epsilon_{I,p}$ 
14      end
15      else if  $\chi_p \neq 1$  and  $\epsilon_{f,p} > 0$  then
16         $\chi_p^{k+1} \leftarrow \min \left\{ 1, \max \left\{ \chi_p^k, \frac{(\epsilon_{I,p} - \epsilon_{f,p}) h_{\epsilon,p}}{w_c} \right\} \right\}$ 
17      end
18    end
19 end

```

Algorithm 2: Compute damage parameter χ

405 **Appendix C. Node-linked method for ϵ -neighbourhood reconstruction**

Input: I_0 : Closest node for each particle
Input: I_{Nodes} : List of nodes close to each node
Input: $Particles_I$: List of particles close to each node
Output: $neighbourhood_\epsilon$: ϵ -neighbourhood for each particle

```

1 for  $p$  to  $N_p$  do
2   For each  $p$  get  $I_0$ 
3   Eval  $I_{Nodes}(I_0)$ 
4   for  $k \in I_{Nodes}(I_0)$  do
5     |  $neighbourhood_\epsilon^{k+1} = neighbourhood_\epsilon^k \cup Particles_I(k)$ 
6   end
7   for  $p_\epsilon \in neighbourhood_\epsilon$  do
8     | if  $distance(p_\epsilon, p) > \epsilon$  then
9       |   | pop  $p_\epsilon$  from  $neighbourhood_\epsilon$ 
10    end
11  end
12 end

```

Algorithm 3: ϵ -neighborhood reconstruction algorithm

References

- [1] G. Barenblatt, The mathematical theory of equilibrium cracks in brittle fracture., Advances in Applied Mechanics 7 (1962) 55–129.
410 doi:10.1016/S0065-2156(08)70121-2.
- [2] A. Hillerborg, M. Modéer, P. Petersson, Analysis of crack formation and crack growth in concrete by means of fracture mechanics and finite elements., Cement and Concrete Research. 6 (1976) 773–782.
415 doi:10.1016/0008-8846(76)90007-7.
- [3] M. Ortiz, A. Pandolfi, Finite-deformation irreversible cohesive elements for three-dimensional crack-propagation analysis., International Journal for Numerical Methods in Engineering. 44 (1999) 1267–1282. doi:10.1002/(SICI)1097-0207(19990330)44:9;1267::AID-NME486;3.0.CO;2-7.
420
- [4] A. Pandolfi, M. Ortiz, An efficient adaptive procedure for three-dimensional fragmentation simulations., Engineering with Computers. 18(2) (2002) 148–159. doi:10.1007/s003660200013.

- 425 [5] G. Ruiz, M. Ortiz, A. Pandolfi, Three-dimensional finite-element simulation of the dynamic Brazilian tests on concrete cylinders, International Journal for Numerical Methods in Engineering 48 (2000) 963–994. doi:10.1002/(SICI)1097-0207(20000710)48:7;963::AID-NME908;3.0.CO;2-X.
- 430 [6] T. Belytschko, H. Chen, J. Xu, G. Zi, Dynamic crack propagation based on loss of hyperbolicity and a new discontinuous enrichment., International Journal for Numerical Methods in Engineering. 58 (2003) 1873–1905. doi:10.1002/nme.941.
- 435 [7] J. Huang, An efficient morphology generation and level set representation of cementitious microstructures with arbitrarily shaped aggregates and cracks via extended finite elements, Computers & Structures 206 (2018) 122 – 144. doi:10.1016/j.compstruc.2018.05.010.
- 440 [8] T. Nagashima, M. Sawada, Development of a damage propagation analysis system based on level set xfem using the cohesive zone model, Computers & Structures 174 (2016) 42 – 53. doi:10.1016/j.compstruc.2015.10.005.
- [9] K. Yun, Z. Wang, M. Chang, J. Liu, T.-J. Kim, N. Son, K. Ji, S. Ronald, A computational methodology for simulating quasi-brittle fracture problems, Computers & Structures 215 (2019) 65 – 79. doi:10.1016/j.compstruc.2019.02.003.
- 445 [10] H. Schreyer, D. Sulsky, S. Zhou, Modeling delamination as a strong discontinuity with the material point method, Computer Methods in Applied Mechanics and Engineering 191 (2002) 2483–2507. doi:10.1016/S0045-7825(01)00409-1.
- 450 [11] Z. Chen, W. Hu, L. Shen, X. An, R. Brannon, An evaluation of the mpm for simulating dynamic failure with damage diffusion, Engineering Fracture Mechanics 69 (2002) 1873–1890. doi:10.1016/S0013-7944(02)00066-8.
- 455 [12] J. Nairn, Material point method calculations with explicit cracks, Computer Modeling in Engineering & Sciences 4 (6) (2003) 649–664. doi:10.3970/cmes.2003.004.649.
- [13] Z. Chen, L. Shen, Y.-W. Mai, Y.-G. Shen, A bifurcation-based decohesion model for simulating the transition from localization to decohesion with the mpm, Zeitschrift fur Angewandte Mathematik und Physik 56 (2005) 908–930. doi:10.1007/s00033-005-3011-0.

- 460 [14] T. Belytschko, Y. Lu, L. Gu, M. Tabbara, Element-free galerkin methods for static and dynamic fracture, *International Journal of Solids and Structures* 32 (17) (1995) 2547 – 2570. doi:10.1016/0020-7683(94)00282-2.
- 465 [15] T. Belytschko, D. Organ, C. Gerlach, Element-free galerkin methods for dynamic fracture in concrete, *Computer Methods in Applied Mechanics and Engineering* 187 (3) (2000) 385 – 399. doi:10.1016/S0045-7825(00)80002-X.
- 470 [16] X. Zhuang, C. Augarde, K. Mathisen, Fracture modeling using meshless methods and level sets in 3d: Framework and modeling, *International Journal for Numerical Methods in Engineering* 92 (2012) 969–998. doi:10.1002/nme.4365.
- 475 [17] N. Muthu, S. Maiti, B. Falzon, I. Guiamatsia, A comparison of stress intensity factors obtained through crack closure integral and other approaches using extended element-free galerkin method, *Computational Mechanics* 52. doi:10.1007/s00466-013-0834-y.
- 480 [18] Y. Wang, H. T. Tran, G. D. Nguyen, P. G. Ranjith, H. H. Bui, Simulation of mixed-mode fracture using sph particles with an embedded fracture process zone, *International Journal for Numerical and Analytical Methods in Geomechanics* 44 (10) (2020) 1417–1445. doi:10.1002/nag.3069.
- 485 [19] Y. Wang, H. Bui, G. Nguyen, P. Ranjith, A new sph-based continuum framework with an embedded fracture process zone for modelling rock fracture, *International Journal of Solids and Structures* 159 (2019) 40–57. doi:10.1016/j.ijsolstr.2018.09.019.
- 490 [20] B. Li, F. Habbal, M. Ortiz, Optimal transportation meshfree approximation schemes for fluid and plastic flows, *International Journal for Numerical Methods in Engineering* 83 (12) (2010) 1541–1579. doi:10.1002/nme.2869.
- 495 [21] B. Li, A. Kadane, G. Ravichandran, M. Ortiz, Verification and validation of the optimal-transportation meshfree (otm) simulation of terminal ballistics., *International Journal for Impact Engineering* 42 (2012) 25–36. doi:10.1016/j.ijimpeng.2011.11.003.
- [22] A. Pandolfi, B. Li, M. Ortiz, Modeling fracture by material-point erosion., *International Journal of fracture* 184 (2013) 3–16. doi:10.1007/s10704-012-9788-x.

- [23] B. Li, A. Pandolfi, M. Ortiz, Material-point erosion simulation of dynamic fragmentation of metals., *Mechanics of Materials* 80 (2015) 288–297. doi:10.1016/j.mechmat.2014.03.008.
- [24] Y. D. Ha, F. Bobaru, Characteristics of dynamic brittle fracture captured with peridynamics, *Engineering Fracture Mechanics* 78 (6) (2011) 1156 – 1168. doi:10.1016/j.engfracmech.2010.11.020.
- [25] T. Rabczuk, H. Ren, A peridynamics formulation for quasi-static fracture and contact in rock, *Engineering Geology* 225 (2017) 42 – 48, special Issue: Characterisation of Fractures in Rock: from Theory to Practice (ROCKFRAC). doi:10.1016/j.enggeo.2017.05.001.
- [26] Y. Guo, J. Nairn, Three-dimensional dynamic fracture analysis using the material point method, *Computer Modeling in Engineering & Sciences* 1 (1) (2006) 11–25. doi:10.3970/cmes.2006.016.141.
- [27] H. Tan, J. Nairn, Hierarchical, adaptive, material point method for dynamic energy release rate calculations, *Computer Methods in Applied Mechanics and Engineering* 191 (2002) 2123–2137. doi:10.1016/S0045-7825(01)00377-2.
- [28] Y. Guo, J. Nairn, Calculation of j-integral and stress intensity factors using the material point method, *CMES. Computer Modeling in Engineering & Sciences* 6 (3) (2004) 295–308. doi:10.3970/cmes.2004.006.295.
- [29] Z. Chen, R. Feng, X. An, L. Shen, A computational model for impact failure with shear-induced dilatancy, *International Journal for Numerical Methods in Engineering* 56 (2003) 1979 – 1997. doi:10.1002/nme.651.
- [30] S. DL, L. Schreyer, Mpm simulation of dynamic material failure with a decohesion constitutive model, *European Journal of Mechanics - A/Solids* 23 (2004) 423–445. doi:10.1016/j.euromechsol.2004.02.007.
- [31] B. Schmidt, F. Fraternali, M. Ortiz, Eigenfracture: an eigendeformation approach to variational fracture., *SIAM J. Multiscale Model. Simul.* 7 (2009) 1237–1266. doi:10.1137/080712568.
- [32] A. Pandolfi, M. Ortiz, An eigenerosion approach to brittle fracture., *International Journal for Numerical Methods in Engineering* 92 (2012) 694–714. doi:10.1002/nme.4352.
- [33] K. Zhang, S.-L. Shen, A. Zhou, Dynamic brittle fracture with eigenerosion enhanced material point method, *International Journal for Numerical Methods in Engineering* (2020) 1–27doi:10.1002/nme.6381.

- [34] P. Navas, R. Yu, B. Li, G. Ruiz, Modeling the dynamic fracture in concrete: an eigensoftening meshfree approach, *International Journal of Impact Engineering* 113. doi:10.1016/j.ijimpeng.2017.11.004.
- [35] P. Navas, S. López-Querol, R. C. Yu, M. Pastor, Optimal transportation meshfree method in geotechnical engineering problems under large deformation regime, *International Journal for Numerical Methods in Engineering* 115 (10) (2018) 1217–1240. doi:10.1002/nme.5841.
- [36] Z. Bažant, B. Oh, Crack band theory for fracture in concrete., *Materials and Structures*. 16 (1983) 155–177. doi:10.1007/BF02486267.
- [37] M. Molinos, P. Navas, M. Pastor, M. Martín Stickle, On the dynamic assessment of the Local-Maximum Entropy Material Point Method through an Explicit Predictor-Corrector Scheme, *Computer Methods in Applied Mechanics and Engineering* Under review (2020) –.
- [38] M. Arroyo, M. Ortiz, Local maximum-entropy approximation schemes: A seamless bridge between finite elements and meshfree methods, *International Journal for Numerical Methods in Engineering* 65 (13) (2006) 2167–2202. doi:10.1002/nme.1534.
- [39] D. L. Sulsky, H. Schreyer, Z. Chen, A particle method for history-dependent materials, *Computer Methods in Applied Mechanics and Engineering* 118 (1) (1994) 179–196. doi:10.1016/0045-7825(94)90112-0.
- [40] E. Jaynes, Information Theory and Statistical Mechanics, *The Physical Review* 106 (4) (1957) 620–630. doi:10.1103/PhysRev.106.620.
- [41] C. E. Shannon, A Mathematical Theory of Communication, *Bell System Technical Journal* 27 (3) (1948) 379–423. doi:10.1002/j.1538-7305.1948.tb01338.x.
- [42] P. Navas, R. Yu, G. Ruiz, Meshfree modeling of the dynamic mixed-mode fracture in frc through an eigensoftening approach, *Engineering Structures* 172 (2018) 94 – 104. doi:10.1016/j.engstruct.2018.06.010.
- [43] M. P. Allen, D. J. Tildesley, *Computer Simulation of Liquids*, Clarendon Press, USA, 1989.
- [44] M. Shimrat, Algorithm 112: Position of point relative to polygon, *Commun. ACM* 5 (8) (1962) 434. doi:10.1145/368637.368653.

- [45] M. Galetzka, P. O. Glauner, A correct even-odd algorithm for the point-in-polygon (PIP) problem for complex polygons, CoRR abs/1207.3502. arXiv:1207.3502.
 URL <http://arxiv.org/abs/1207.3502>
- [46] E. Wobbes, R. Tielen, M. Möller, C. Vuik, Comparison and unification of material-point and optimal transportation meshfree methods, Computational Particle Mechanics doi:10.1007/s40571-020-00316-7.
- [47] S. G. S. G. Bardenhagen, E. M. Kober, The generalized interpolation material point method, CMES - Computer Modeling in Engineering and Sciences 5 (6) (2004) 477–495.
- [48] I. Lim, I. Johnston, S. Choi, Stress intensity factors for semi-circular specimens under three-point bending, Engineering Fracture Mechanics 44 (3) (1993) 363 – 382. doi:10.1016/0013-7944(93)90030-V.
- [49] X. Zhang, G. Ruiz, R. Yu, M. Tarifa, Fracture behaviour of high-strength concrete at a wide range of loading rates., International Journal of Impact Engineering 36 (2009) 1204–1209. doi:10.1016/j.ijimpeng.2009.04.007.
- [50] X. Zhang, R. Yu, G. Ruiz, M. Tarifa, M. Camara, Effect of loading rate on crack velocities in hsc., International Journal of Impact Engineering 37 (2010) 359–370. doi:10.1016/j.ijimpeng.2009.10.002.
- [51] S. Bardenhagen, J. Guilkey, K. Roessig, J. Brackbill, W. Witzel, J. Foster, An improved contact algorithm for the material point method and application to stress propagation in granular material, CMES. Computer Modeling in Engineering & Sciences 2 (4) (2001) 509–522. doi:10.3970/cmes.2001.002.509.
- [52] P. Huang, X. Zhang, S. Ma, X. Huang, Contact algorithms for the material point method in impact and penetration simulation, International Journal for Numerical Methods in Engineering 85 (2011) 498 – 517. doi:10.1002/nme.2981.
- [53] G. Ruiz, A. de la Rosa, L. Almeida, E. Poveda, X. Zhang, M. Tarifa, Z. Wu, R. Yu, Dynamic mixed-mode fracture in scc reinforced with steel fibers: an experimental study, International Journal of Impact Engineering 129 (2019) 101 – 111. doi:<https://doi.org/10.1016/j.ijimpeng.2019.03.003>.

- [54] K. Wang, W. Sun, A unified variational eigen-erosion framework for interacting brittle fractures and compaction bands in fluid-infiltrating porous media, Computer Methods in Applied Mechanics & Engineering 318 (2017) 1 – 32. doi:10.1016/j.cma.2017.01.017.
- [55] S. Kumar, K. Danas, D. M. Kochmann, Enhanced local maximum-entropy approximation for stable meshfree simulations, Computer Methods in Applied Mechanics and Engineering 344 (2019) 858 – 886. doi:10.1016/j.cma.2018.10.030.